J. Fluid Mech. (1985), *vol.* 152, *pp.* 235–248
Printed in Great Britain

On flow visualization using reflective flakes

By Ö. SAVAŞ

School of Aerospace, Mechanical, and Nuclear Engineering, University of Oklahoma, Norman, OK 73019

(Received 21 February 1984 and in revised form 28 September 1984)

An analysis of flow visualization using small reflective flakes is introduced. This rational analysis is based on a stochastic treatment of Jeffery's (1922) solution for the motion of ellipsoidal particles in a viscous fluid, wherein thin flakes tend to align with stream surfaces. The predicted light fields are confirmed by examples of parallel flows, the flow over a rotating disk, and the spinup from rest in a cylindrical cavity. The Tollmien–Schlichting wave packet trailing a turbulent spot is taken as an example to discuss the suitability of the technique for visualizing small-amplitude waves. Attenuation of light through a suspension is described.

1. Introduction

A few pleasant moments spent leafing through Van Dyke's (1982) album should be enough to convince anyone of the power of flow visualization in unveiling the beauties of fluid flow. The flow field reveals itself through either some changes of the properties of fluid as it flows or some visualization agents introduced into it. Of the numerous individual techniques, visualization through the use of small reflective flakes, such as aluminium flakes, titanium-dioxide-coated mica platelets, or fish flakes, seems to be least understood. The commonly quoted view that such flakes align themselves along the axes of principal normal stresses in the flow field is unsubstantiated (see, for example, Carlson, Widnall & Peeters 1982). The purpose of this article is to present a rational analysis of the nature of flow visualization using such flakes. Examples are presented to demonstrate the applicability of the analysis.

The analysis is based on Jeffery's solution of the motion of ellipsoidal particles immersed in a viscous fluid. This solution has been experimentally verified by Goldsmith & Mason (1962). Greenspan, in an appendix published by Weidman (1976), uses this solution to estimate the response time of aluminum flakes during spinup in a cylindrical cavity. Weidman further concludes that both velocity and its time derivative are vanishingly small when aluminum flakes first sense the approaching disturbance. No other quantitative treatment of the technique appears to be currently available in the literature.

2. Principle of visualization

2.1. *Flake in flow field*

An individual flake is idealized as a thin buoyant circular disk of a suitably defined thickness-to-diameter ratio ρ. Its normal unit vector $\boldsymbol{n}$ is used to specify its orientation in space. Let the flake be at the origin O of the (x,y,z)-coordinate system (figure 1). The Euler angles of $\boldsymbol{n}$ are θ and ϕ. Let a uniform light beam come from L and an observer be at C. Let the unit vectors $\boldsymbol{n}_1 = (l,m,n)_1$, $\boldsymbol{n} = (l,m,n)$, and

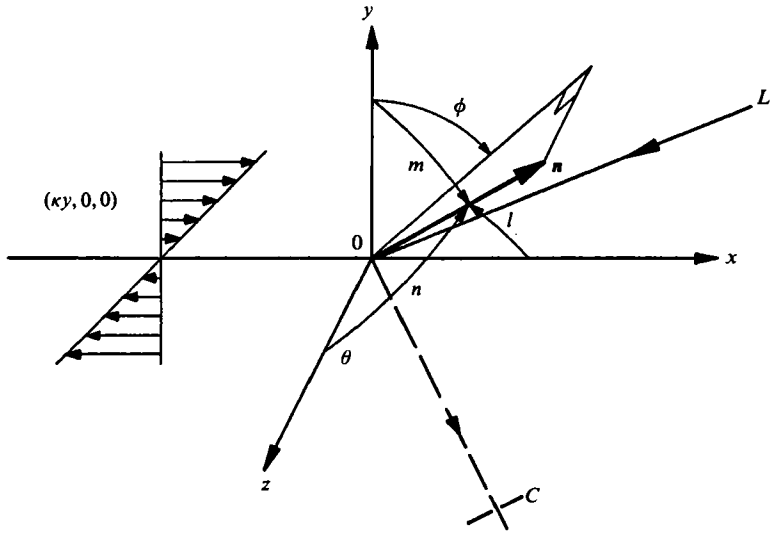

FIGURE 1. Reflective flake in shear flow. Reference system and visualization geometry. L, light source, O, flake, C, camera. Note that ϕ is measured in xy plane between y axis and projection of $\boldsymbol{n}$.

$\boldsymbol{n}_c = (l, m, n)_c$ describe the relative orientations of the light source, the flake, and the observer; where l, m and n are the direction cosines with respect to the x, y, and z axes. Note that $\boldsymbol{n} = (\sin\theta \sin\phi, \sin\theta \cos\phi, \cos\theta)$. Assuming the flake to be perfectly flat with negligible diffraction and the observer to be a pinhole camera, then the normal vector of the flake $\boldsymbol{n}$ has to be the bisector of the angle LOC in order for the observer to see the reflected light. This geometric requirement leads to a unique relationship between the direction cosines of the three vectors,

$$\cos^2\theta^* = \frac{(n_l + n_c)^2}{(l_l + l_c)^2 + (m_l + m_c)^2 + (n_l + n_c)^2} \tag{1}$$

and

$$\cos^2\phi^* = \frac{(m_l + m_c)^2}{(l_l + l_c)^2 + (m_l + m_c)^2}, \tag{2}$$

where (*) labels the condition when the observer sees light.

Consider the flake with a velocity field $\boldsymbol{U}$ in an inertial coordinate system. Apart from the disturbance produced in the immediate neighbourhood of the flake, assume the flow field varies on a spatial scale that is large compared to the dimensions of the flake. Consequently, the Reynolds number for the flake is small and it assumes the translation velocity appropriate to that part of the replaced fluid. This velocity $\boldsymbol{U}_f$ is sensibly uniform, and the centre of the particle may therefore be taken as the origin of an inertial coordinate system. Let the xyz-coordinate system be such an inertial reference frame. The undisturbed field in the vicinity of the flake can be approximated as (Batchelor 1967)

$$u_i = e_{ij} x_j + \tfrac{1}{2}\boldsymbol{\omega} \times \boldsymbol{x},$$

where $\boldsymbol{u} = \boldsymbol{U} - \boldsymbol{U}_f$, and e_{ij}, $\boldsymbol{\omega}$, and $\boldsymbol{x}$ are the rate-of-strain tensor, vorticity, and the position vectors, respectively. A parallel flow is chosen because the equations governing the motion of the disk can be integrated analytically (Jeffery),

$$(u, v, w) = [\kappa(t)\, y, 0, 0], \tag{3}$$

where the coefficient κ may depend on time (figure 1). The timescale of the flow is assumed to be smaller than that of the randomizing effects of the Brownian motion on the flakes. The corresponding strain-rate tensor and vorticity vector are

$$e_{ij} = \begin{pmatrix} 0 & \frac{1}{2}\kappa & 0 \\ \frac{1}{2}\kappa & 0 & 0 \\ 0 & 0 & 0 \end{pmatrix} \tag{4}$$

and

$$\omega = (0, 0, -\kappa).$$

The principal axes of strain is arrived at by rotating the xyz system 45° around the z axis.

2.2. *Motion of a flake*

Under the assumptions already stated, the motion of the flake is described by the following equations derived by Jeffery

$$\frac{\mathrm{d}\theta}{\mathrm{d}t} = -\tfrac{1}{4}\kappa(t)\frac{1-\rho^2}{1+\rho^2}\sin 2\theta \sin 2\phi$$

and

$$\frac{\mathrm{d}\phi}{\mathrm{d}t} = \frac{\kappa(t)}{1+\rho^2}(\sin^2\phi + \rho^2\cos^2\phi).$$

The initial conditions are

$$\theta(0) = \theta_0 \quad \text{and} \quad \phi(0) = \phi_0.$$

These equations are integrated to yield

$$\frac{\tan^2\theta}{\tan^2\theta_0} = \frac{\sin^2\phi_0 + \rho^2\cos^2\phi_0}{\sin^2\phi + \rho^2\cos^2\phi} \tag{5}$$

and

$$\tan^{-1}\left(\frac{1}{\rho}\tan\phi\right) - \tan^{-1}\left(\frac{1}{\rho}\tan\phi_0\right) = \frac{\rho}{1+\rho^2}S(t), \tag{6}$$

where

$$S(t) = \int_0^t \kappa(\xi)\,\mathrm{d}\xi. \tag{7}$$

Hence, the orientation at time t depends only on ρ, $S(t)$, and the initial Euler angles. Clearly, when $S \to 0$, the Euler angles remain at their initial values.

2.3. *Visualization*

Consider a large number of flakes with a uniform concentration in the flow field. While a deterministic approach is no longer feasible, some important statistical properties of the suspension can be obtained easily by using the probability-density function $f(\theta, \phi)$. Flow visualization using reflective flakes is essentially a means of displaying $f(\theta, \phi)$ optically in space and time. The correct interpretation of such visualizations must necessarily involve the evolution of the probability density function $f(\theta, \phi)$. The essence of this article is that the initial values θ_0 and ϕ_0 are treated as random variables and θ and ϕ as functions of these two random variables, that is:

$$\theta = \theta(\theta_0, \phi_0) \quad \text{and} \quad \phi = \phi(\theta_0, \phi_0).$$

The evolution of $f(\theta, \phi)$ is described by Papoulis (1984) as

$$f(\theta, \phi) = \frac{f_0(\theta_0, \phi_0)}{J}, \tag{8a}$$

where $f_0(\theta_0, \phi_0)$ is the initial probability density function of the random variables θ_0 and ϕ_0, and J is the Jacobian $\partial(\theta, \phi)/\partial(\theta_0, \phi_0)$. It is evaluated with (5) and (6) as

$$J(\theta, \phi, t) = Q^{\frac{1}{2}}(\cos^2\theta + Q\sin^2\theta), \tag{8b}$$

where

$$Q(\phi, t) = (\sin^2\phi + \rho^2\cos^2\phi)\left(\sin^2\Phi + \frac{1}{\rho^2}\cos^2\Phi\right) \tag{8c}$$

and

$$\Phi(\phi, t) = \tan^{-1}\left(\frac{1}{\rho}\tan\phi\right) - \frac{\rho}{1+\rho^2}S(t). \tag{8d}$$

The observer in figure 1 thus sees $f(\theta^*, \phi^*)$ where θ^* and ϕ^* are given by (1) and (2). Note that $J > 0$.

Jeffery and Goldsmith & Mason describe the motion of an individual particle. The finite thickness of the flake ρ causes it to rotate and flip over. This motion is periodic if $\kappa(t)$ is constant. The flake spends most of its time near alignment with stream surfaces and flips over rapidly when at large angle to the flow (see figure 5 of Goldsmith & Mason). An observer looking at a flake in a steady shear flow under diffuse illumination therefore sees a smooth translation interrupted by sudden turnovers, as Coles (1965) observed under a microscope. In the limiting case of zero thickness, the motion is no longer periodic. The flake takes the unique position in which its faces are aligned with the stream surfaces of the undisturbed motion. It thus moves through the fluid edge-on with its axis at a given inclination to the shear, not necessarily along the principal strain directions of (4). Equation (8) then becomes

$$f(\theta, \phi) = \frac{f_0(\theta_0, \phi_0)}{Q^{\frac{1}{2}}(\cos^2\theta + Q\sin^2\theta)}, \tag{9}$$

where

$$Q(\phi, t) = \sin^2\phi + [\cos\phi + \sin\phi\, S(t)]^2. \tag{10}$$

Equation (9) contains all the important features needed to describe visualizations in flow fields for which (3) is an acceptable local approximation. Note that $f = f_0$ when $S(t) = 0$.

3. Examples

The following examples are presented to demonstrate the applicability of the principle of flow visualization developed in the preceding section. Before considering each case, the Brownian timescale of the flow has to be considered. Leal & Hinch (1971, 1972) describe the behaviour of dilute suspensions subject to Brownian couples. They conclude that the suspension has an exponentially fading memory with a characteristic timescale of $(6D)^{-1}$, where D is the Brownian orientation diffusion coefficient. This timescale is $(4/3\pi)(\mu V/\rho kT)$ as $\rho \to 0$, where μ, V, k, and T are the viscosity of the fluid, the volume of a typical flake, the Boltzmann constant (1.380×10^{-16} erg/K), and the absolute temperature, respectively. A typical flake is ~ 1 μm thick and ~ 10 μm wide, thus, its volume is $\sim 10^{-10}$ cm^3 and $\rho \sim 0.1$. The Brownian timescale at room temperature is ~ 100 s in water and ~ 1000 s in silicone oil used in the spinup example. These timescales are much larger than those of the respective flows so that the effect of Brownian motion during the flow can be neglected.

3.1. *Parallel flow*

Suppose the flow commences from a state where $f_0(\theta_0, \phi_0) = 1$, that is all orientations are equally possible resulting in a uniform light field when observed from any direction under any uniform illumination (f_0 is normalized to 4π). Such a state can be attained if the fluid stays in a shear-free state long enough for Brownian motion to randomize any nonuniformity. As the flow experiences a shearing action, the orientation of the flakes is described by

$$f(\theta, \phi) = \frac{1}{Q^{\frac{1}{2}}(\cos^2\theta + Q\sin^2\theta)}. \tag{11}$$

It is apparent from (10) and (11) that $f(\theta, \phi)$ is vanishingly small when $S(t) \to \infty$ except when $\tan 2\phi$ is near $-2/S$. When $\tan 2\phi \to -2/S$, $f(\theta, \phi) \to S/(\cos^2\theta + \sin^2\theta/S^2)$. Thus, the observer sees the flakes aligned with the stream surfaces in the xz-plane, and

$$f(\theta, \phi) \to 2\pi\delta(\theta - \tfrac{1}{2}\pi, \phi) \quad \text{as } S \to \infty, \tag{12}$$

where the delta function δ is introduced as a symbolic representation for the limiting process. If the flakes experience no shear, then $f(\theta, \phi)$ does not change. Such cases are readily observable in boundary layers and channel flows. Flakes away from the boundary do not change their orientations while the ones undergoing shearing realign themselves. For example, the flakes are aligned parallel to the wall in a laminar boundary layer. If such a layer is illuminated with a light sheet perpendicular to the flow, an observer looking along the direction of the flow will see a dark band over the wall whose width is indicative of the local boundary-layer thickness. This width can be calculated from (11) for the particular flow.

The following desk-top experiment in laminar pipe flow should be helpful to demonstrate the validity of the arguments presented here. Suspend in a beaker of water some aluminium flakes or frosty eye shadow makeup which contains titanium-dioxide-coated mica flakes. Some detergent may be necessary to wet the flakes. Then slowly siphon the fluid through a clear, small-diameter plastic tubing while observing under a magnifying glass or a microscope the behaviour of the flakes. The orientations of the flakes are different along the centreline of the tubing than elsewhere. One notices that at the centre of the tubing the distribution of the orientations of the flakes hardly differs from those in the beaker [$f(\theta, \phi) \approx f_0(\theta_0, \phi_0)$], while the ones away from the centre tend to align themselves with their normals perpendicular to the axis of the tubing ($\theta \to \frac{1}{2}\pi$, $\phi \to 0$ in figure 1, equation (12)).

3.2. *Flow over a rotating disk: Kármán flow*

Consider the flow over a rotating disk in a quiescent fluid. The components of the velocity vector $\boldsymbol{U}$ in the usual cylindrical coordinates are

$$(U, V, W) = [r\Omega F(\eta),\ r\Omega G(\eta),\ (\nu\Omega)^{\frac{1}{2}} H(\eta)]$$

with $\eta \equiv y(\Omega/\nu)^{\frac{1}{2}}$, where r, Ω, ν, and y are the radial coordinate, the angular velocity, the kinematic viscosity, and the axial coordinate, respectively. The functions F, G, and H are determined from equations of the flow. They are shown in figure 2 for reference. The corresponding strain-rate tensor is

$$\begin{pmatrix} e_{rr} & e_{r\theta} & e_{ry} \\ e_{\theta r} & e_{\theta\theta} & e_{\theta y} \\ e_{yr} & e_{y\theta} & e_{yy} \end{pmatrix} = \tfrac{1}{2}\Omega E_r^{-\frac{1}{2}} \begin{pmatrix} 2E_r^{\frac{1}{2}} F & 0 & F' \\ 0 & 2E_r^{\frac{1}{2}} F & G' \\ F' & G' & 2E_r^{\frac{1}{2}} H' \end{pmatrix}$$

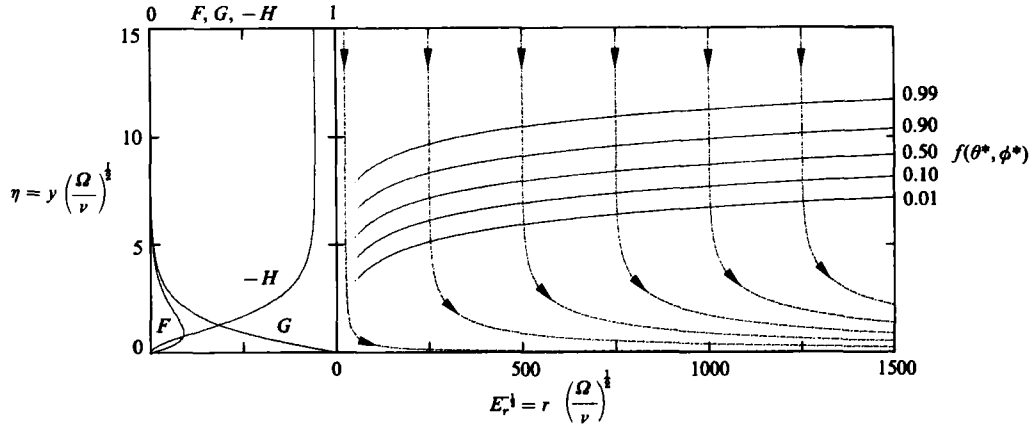

FIGURE 2. Kármán flow; velocity profiles, pathlines and $f(\theta^*, \phi^*)$. Constant $f(\theta^*, \phi^*)$ contours, $\eta = 1.1306 \ln E_r^{-\frac{1}{2}} + \text{constant}$, are drawn for $\rho = 0$ (cf. Greenspan, figure 1.4).

where E_r is the local Ekman number $\nu/\Omega r^2$. Suppose the quiescent fluid contains reflective flakes in a uniform suspension with $f_0(\theta_0, \phi_0) = 1$. Let a thin sheet of light illuminate the flow field diametrically (through the axis of rotation). The light field seen by an observer looking perpendicular to the sheet can be calculated analytically from (8) for $E_r \ll 1$ far from the disk, and where

$$(F, G, H) \sim (F_0 \mathrm{e}^{-c\eta}, G_0 \mathrm{e}^{-c\eta}, -c),$$

with

$$(F_0, G_0, c) = (0.91772, 1.20211, 0.88446)$$

from Rogers & Lance (1960). The local flow field can be approximated by (3) with

$$\kappa = -c(F_0^2 + G_0^2)^{\frac{1}{2}} \Omega E_r^{-\frac{1}{2}} \mathrm{e}^{-c\eta},$$

if the x axis is chosen along the direction of the vector (U, V, O). Note that the xyz coordinate system moves with the flake along the pathline ($U_f = U$), and its orientation continually changes with respect to the observer. Taking $t \to 0$ as $y \to \infty$, the integral S is evaluated along a pathline as

$$S = -\frac{1}{c}(F_0^2 + G_0^2)^{\frac{1}{2}} E_r^{-\frac{1}{2}} \mathrm{e}^{-c\eta}.$$

The observation angles are $|\theta^*| = \frac{1}{4}\pi + \tan^{-1}(G_0/F_0)$ and $\phi^* = \frac{1}{2}\pi$ from (1) and (2). The final result is

$$f(\theta^*, \phi^*) = 2(F_0^2 + G_0^2) Q^{-\frac{1}{2}} [(F_0 - G_0)^2 + (F_0 + G_0)^2 Q]^{-1},$$

where

$$Q = 1 + \left(\frac{1}{\rho^2} - 1\right) \sin^2\left(\frac{\rho}{1+\rho^2} S\right).$$

Thus, constant $f(\theta^*, \phi^*)$ contours are logarithmic curves in the ry-plane. Note that the observed shape is independent of the parameters Ω and ν. Further, the visible width of the boundary layer is progressively thicker than the conventional boundary-layer thickness $5(\nu/\Omega)^{\frac{1}{2}}$. The limiting case for $\rho \to 0$ is

$$f(\theta^*, \phi^*) = (1 + S^2)^{-\frac{1}{2}} \left[1 + \frac{1}{2} \frac{(F_0 + G_0)^2}{F_0^2 + G_0^2} S^2\right]^{-1}.$$

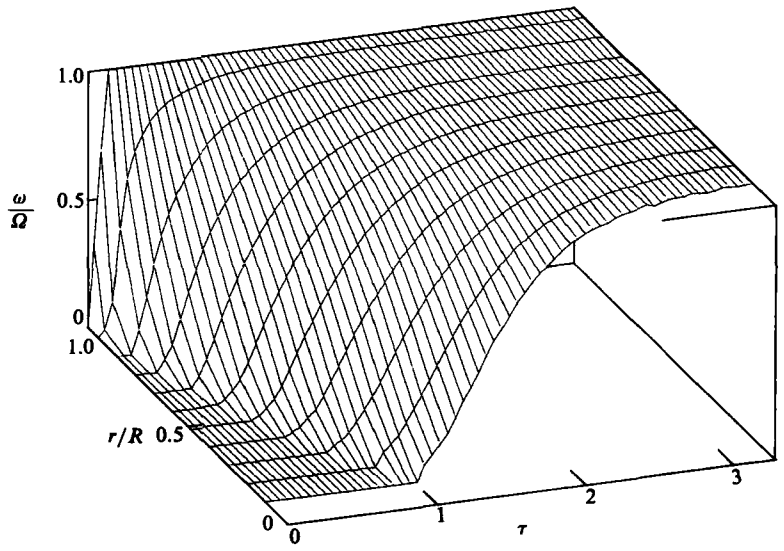

FIGURE 3. Laser-Doppler measurements of spinup from rest in right circular cylindrical cavity of diameter-to-height-ratio of $2R/H = 1.00$. Angular velocity ω/Ω of fluid elements at midheight as a function of time $\tau = (\Omega\nu/H^2)^{\frac{1}{2}}t$ and radius r/R; $\Omega = 17.50$ rad/s at 7.93 rad/s^2, $H = 21.48$ cm, $\nu = 0.102$ cm^2/s.

Some selected contours and pathlines are plotted in figure 2. Even though the shapes shown in figure 2 are similar to that depicted in Greenspan's (1968) figure 1.4, a quantitative comparison is not possible.

3.3. *Spinup from rest*

A more convincing test of the analysis is to compare the predictions of (8) with measurements in a known flow field. The flow in a cylindrical cavity during spinup from rest is used to confirm quantitatively the principle of flow visualization using reflective flakes. A complete set of laser-Doppler velocimeter measurements of the azimuthal velocity at the midplane of the cylinder is available to the author,† as shown in figure 3. The flow is duplicated at the University of Oklahoma for flow-visualization experiments. Aluminium flakes of approximately 40 μm diameter are used at a concentration of about 10 mg of aluminium per litre of silicone oil. A thin sheet of light from a 2 W argon ion laser illuminates the cylinder diametrically through the axis as shown in figure 4. The camera is at a right angle to the plane of illumination so that $\theta^* = \frac{1}{2}\pi$. If the cylinder has been at rest long enough, then $f_0(\theta_0, \phi_0) = 1$ and (8) reduces to

$$f(\theta^*, \phi^*) = \left[(\sin^2\phi^* + \rho^2\cos^2\phi^*)\left(\sin^2\Phi^* + \frac{1}{\rho^2}\cos^2\Phi^*\right)\right]^{-\frac{3}{2}},$$

where

$$\Phi^* = \tan^{-1}\left(\frac{1}{\rho}\tan\phi^*\right) - \frac{\rho}{1+\rho^2}S(t).$$

The angle ϕ^* depends on the radial coordinate r and is determined as indicated in figure 4. The local strain rate $e_{xy} = \frac{1}{2}[\partial(\omega r)/\partial r - \omega]$ is determined from the data of

† Measurements were made in 1976 by Ö. Savaş and D. Coles at The Graduate Aeronautical Laboratories of California Institute of Technology, Pasadena, CA.

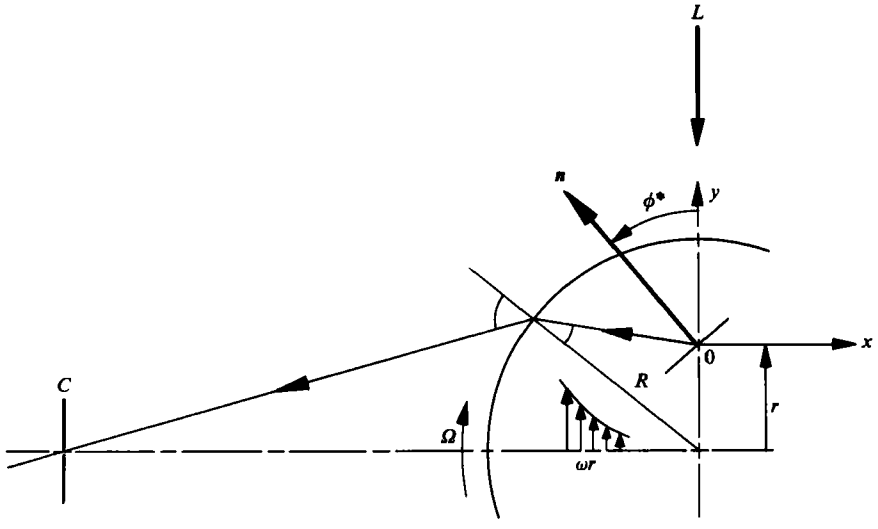

FIGURE 4. Visualization geometry for flow of figure 3. Note the lens effect of the cylindrical cavity. The refractive index of silicone oil is 1.399, $R = 11.37$ cm (including the wall thickness of the cylinder). L, sheet of laser light thinner than 1 mm, C, 35 mm camera.

figure 3 using a second-order finite-difference scheme. This intermediate step is shown in figure 5(*a*) in the form $\kappa(t) = 2e_{xy}$ (cf. (3) and (4)), which is subsequently integrated to obtain $S(t)$ for each radial position. The end product of these calculations is the probability density function $f(\theta^*, \phi^*)$. The result is shown in figure 5(*b*) for $\rho = 0.18$. The reason for choosing $\rho = 0.18$ is discussed below. The intensity of light coming from a given radial location stays nearly constant until changing conditions are felt by the flakes. They reorient themselves so that the amount of light coming from that particular location increases to a well-defined maximum value before decreasing to a vanishingly small level. Alternatively, at any given instant there is a point with maximum light intensity. The region in front of this point is uniformly illuminated, while the region immediately behind it is dark. The trajectory of this first maximum point provides a convenient way of identifying the position of the visible front, as shown in figure 6. This trajectory is insensitive to the value of ρ within the error limits of the measurements. The calculations for $\rho = 0$ using (9) and (10) yield the same trajectory. The peaks following the dark region are due to the finite thickness of the flakes. Their amplitudes and trajectories are strongly dependent on ρ. These secondary peaks are harder to identify than the primary one. The first of such peaks, however, could be identified clearly in the flow-visualization pictures. Greenspan's figure 1.4(*b*) is informative in explaining the important features of the flow, but inadequate for a test of figures 5(*b*) and 6. The pictures presented in figure 7, which are two of many, confirm figure 5(*b*). All the predicted features are present. The observed trajectories for four realizations are shown in figure 6. The predicted trajectory of the first peak and the observations are indistinguishable. The value of ρ is chosen such that the first secondary trajectory from figure 5(*a*) closely approximates the measurements shown in figure 6. Thus, a byproduct of the analysis and the experiments is a novel method to determine the effective thickness ρ of the flakes.

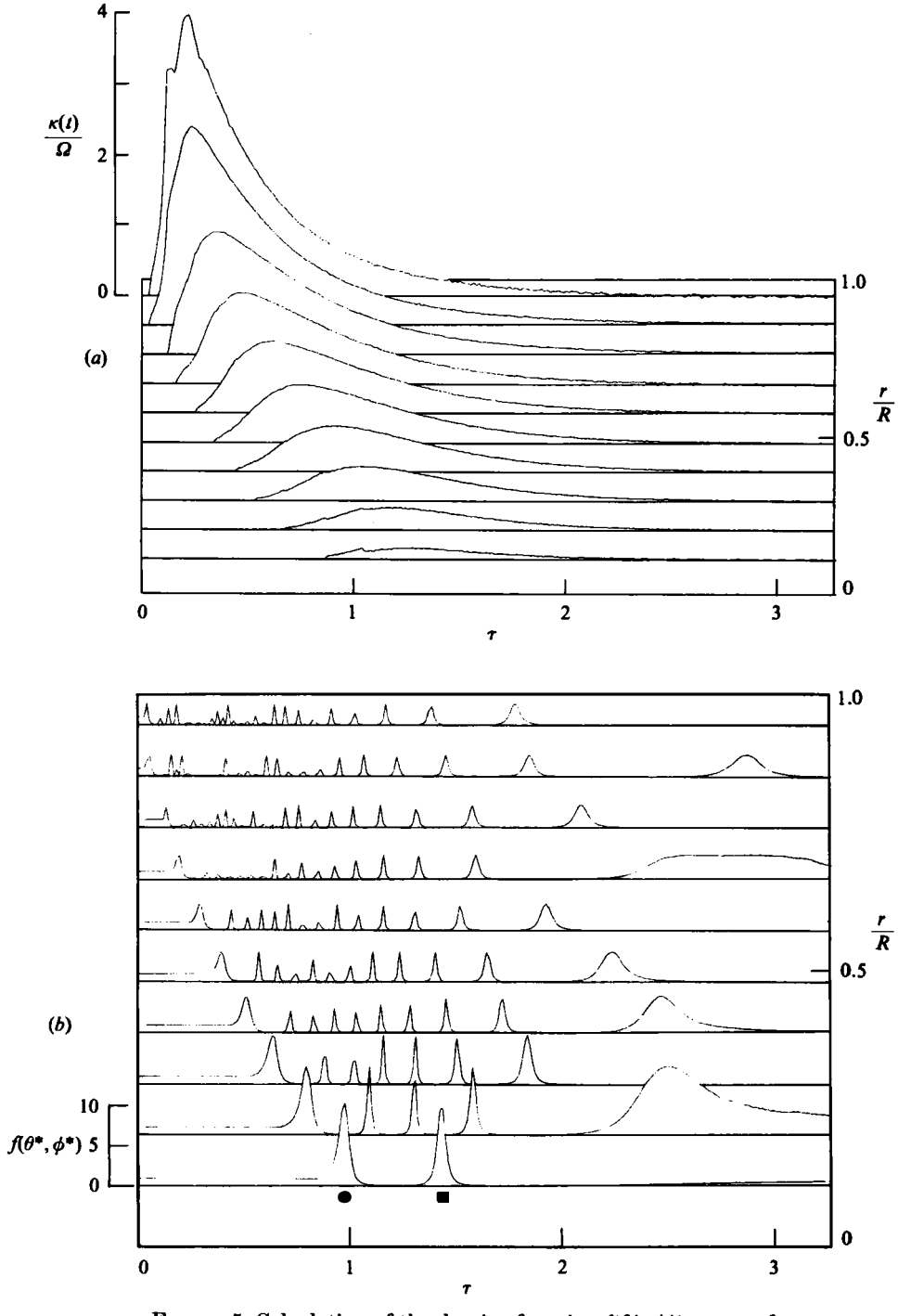

FIGURE 5. Calculation of the density function $f(\theta^*, \phi^*)$ as seen from the geometry of figure 4; (*a*) $\kappa(t)$; (*b*) $f(\theta^*, \phi^*)$ for $\rho = 0.18$.

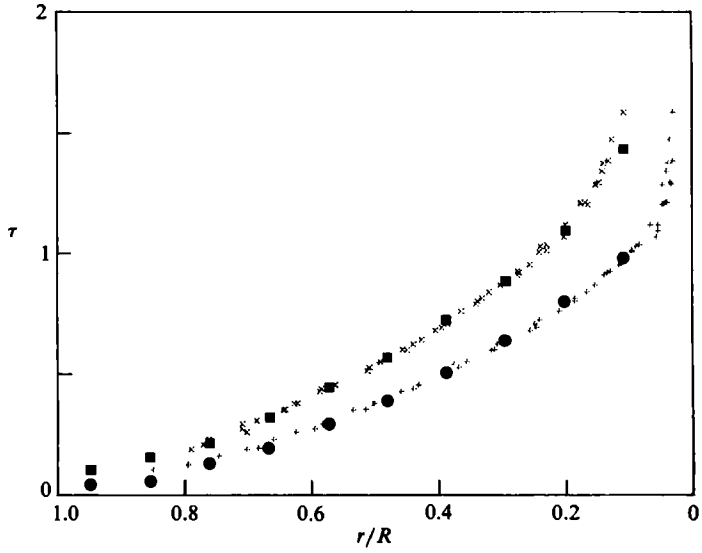

FIGURE 6. Trajectories of the visible peaks of light intensity; ●, ■ from the calculations of figure 5; +, × measurements from photographs such as figure 7.

3.4. *Waves in high shear*

The reflective-flake flow-visualization technique seems to be rather unsuitable for the visualization of low-amplitude shear waves in a unidirectional high-shear flow. If the flow starts from a condition where $f_0(\theta_0, \phi_0) = 1$, then the evolution of the flake distribution is described by (11). During the journey the contribution to the integral $S(t)$ of (7) steadily increases. When the flakes encounter low-amplitude waves, such as Tollmien–Schlichting waves, the new contribution to the integral is extremely small; thus the orientation of the flakes is given by (12) with small oscillations around $\phi = 0$. An alternative approach can be taken with reference to the local conditions. This time consider the flake distribution described by (9) where $f_0(\theta_0, \phi_0)$ is given by (12). The integral $S(t)$ now covers the lifespan of these waves. Their effect is felt when $\phi \neq 0$ because of the factor $\sin\phi$. The form of $f_0(\theta_0, \phi_0)$ however inhibits any such effect from being observed in $f(\theta, \phi)$ of (9). Given the approximate nature of the analysis, changes in ϕ are at best very small oscillations around $\phi = 0$. Therefore the optical arrangement has to be capable of seeing these small angular variations around $\phi = 0$. Such an arrangement is rather demanding.

An instructive example is provided by the wave packets observed in the presence of a turbulent spot. Wygnanski, Haritonidis & Kaplan (1979) reported hot-wire measurements of the oblique wave packets trailing a turbulent spot in a laminar boundary layer. Cantwell, Coles & Dimotakis (1978), who were aware of the preliminary results of Wynganski *et al.*, did not notice these waves in their aluminium flake visualizations during their investigation of the turbulent spot. They argue that their Reynolds number may not have been high enough. Later, visualization studies by Carlson *et al.* in plane Poiseuille flow revealed similar wave phenomena coupled with the turbulent spot. They used titanium-dioxide-coated mica particles at a low concentration, which allowed them to see through the full 6 mm width of their apparatus. Carlson *et al.* argue that Cantwell *et al.* could not have observed the waves because of their opaque suspension which allowed a visible depth of only 2–3 mm (Cantwell *et al.*). Due to the symmetry of their apparatus, however, the effective

(*a*)

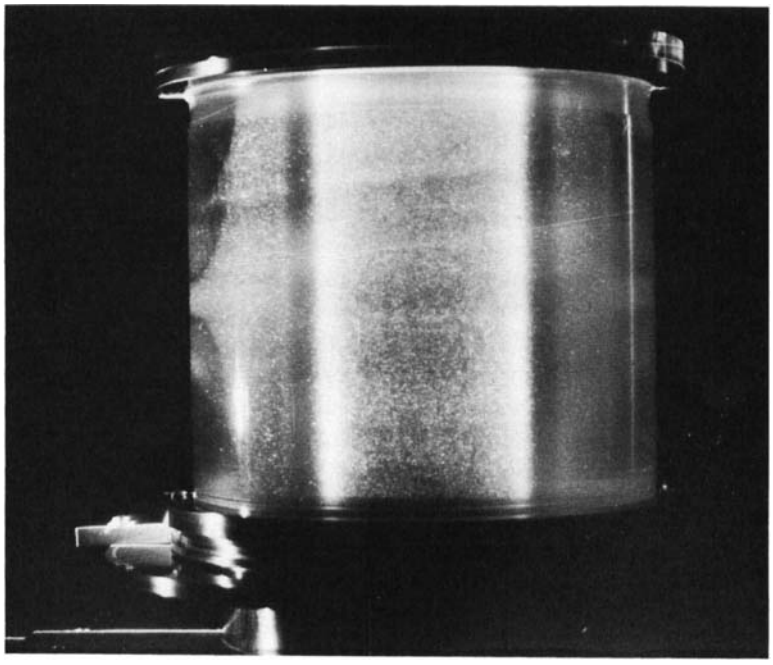

(*b*)

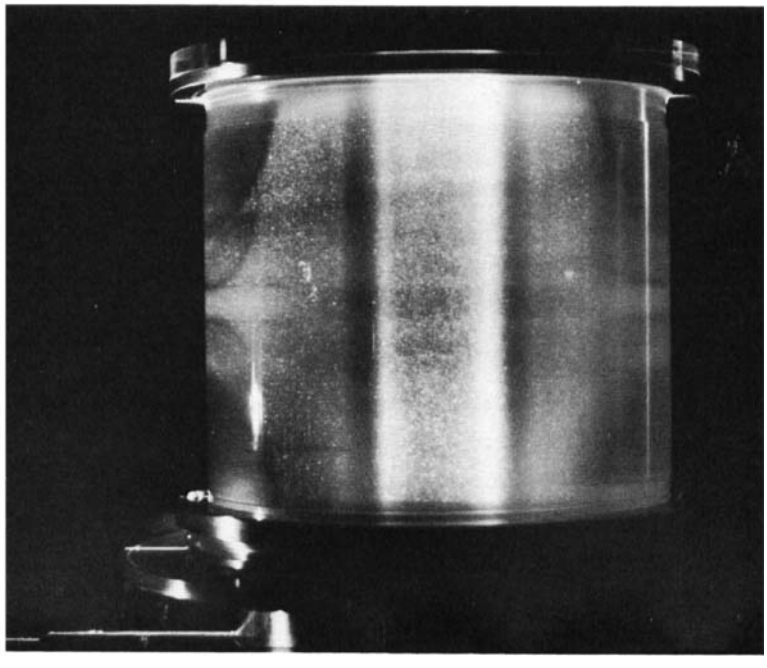

FIGURE 7. Two successive photographs during spinup from rest; (*a*) $t = 9.7$ s; (*b*) $t = 13.6$ s.

visible depth in the Carlson *et al.* experiments is not 6 mm, but 3 mm, which hardly differs from the depth that Cantwell *et al.* could observe. More recently, Chambers & Thomas (1983) have observed these oblique waves in a boundary layer with a smoke-wire visualization technique at low Reynolds numbers that are comparable with those of Cantwell *et al.*

The foregoing conflict is not a question of Reynolds number or of the visible depth. Cantwell *et al.* did not see any evidence of such waves because the way they implemented the flow-visualization technique was not suitable for that purpose. Had they illuminated the boundary layer at a shallow angle, almost parallel to the flow and observed at a shallow angle from the other side, they would have seen the oblique wave packet trailing the turbulent spots in their boundary layer.

A fully developed Poiseuille flow has a parabolic velocity profile with its maximum at the centre where the rate of strain crosses the zero point. The flow in the vicinity of the centre can be approximated as a uniform translation with vanishingly small shear. The value of the integral $S(t)$ is negligible for the flakes in this region. Consequently, the density function $f(\theta, \phi)$ remains the same as $f_0(\theta_0, \phi_0)$, and is thus near unity. Away from the centre the shear continually contributes to $S(t)$, thus aligning the flakes towards the distribution of (12). Within the simplifying assumptions of this article, the density function $f(\theta, \phi)$ tends to (12), except at the centre where it remains as unity. When the flow experiences shear waves the density function responds differently in different regions of the flow. The response of the central part is intense enough to be observed from any direction as the dominant contribution to $S(t)$ comes from these waves. In the remainder of the flow where the shear has built up a large value for $S(t)$, the contribution from the waves is infinitesimal and is difficult to observe except under shallow illumination and observation angles.

Carlson *et al.*'s visualization experiment is an elegant demonstration of these arguments. Even though they used large quantities of flakes, the grainy look of their pictures leads to the impression that the flake concentration was very low. The information that their camera records comes mostly from the central plane of their apparatus where only a small fraction of the flakes are present. The remainder of the flakes are in high-shear regions and are already aligned as described by (12). Thus, most of the flakes are not participating in the visualization. As a consequence of the arguments presented here, if Carlson *et al.* illuminated the central plane of their apparatus with a very thin sheet of light, they would get the same quality pictures, or maybe even better ones, due to the reduced noise level. Conversely, if they illuminated the whole flow field but the central plane, their camera would record little or no wave activity.

3.5. *Light attenuation*

The light transmission characteristics of a suspension containing reflective flakes can be calculated. Suppose the observer C looks directly into the light source L (figure 1). The attenuation of the light intensity recorded at C can provide valuable information about the flow field as well as the suspension itself. A flake of area a_0 deflects a portion of the incoming light beam whose cross-sectional area is the projection of a_0 along $\boldsymbol{n}_1$ given by $a = a_0 |\boldsymbol{n} \cdot \boldsymbol{n}_1|$, and from §2.1,

$$a(\theta, \phi) = a_0 |l_1 \sin\theta \sin\phi + m_1 \sin\theta \cos\phi + n_1 \cos\theta|.$$

The expected value of a is

$$\langle a \rangle = \frac{1}{4\pi} \int_0^{2\pi} \mathrm{d}\phi \int_0^{\pi} \mathrm{d}\theta \sin\theta \, a(\theta, \phi) f(\theta, \phi),$$

where the integration is over the unit sphere and $f(\theta, \phi)$ is given by (8). Thus, $\langle a \rangle$ is the expected amount of light deflected by a flake from the direction of illumination which is recorded as attenuation at C. The total attenuation is obtained by integrating the contributions from the flakes within the path of the light beam.

If the flake concentration is low enough, then the optical interaction among the flakes can be neglected. If, in addition, the suspension is uniform and the flakes are of the same area a_0, then the total attenuation A observed at C is an integral over the volume of the path of the light beam;

$$A = N \iiint_{\mathscr{V}} \langle a \rangle \, \mathrm{d}V,$$

where N is the number of flakes per unit volume. This interpretation can help further understand shadowgraph pictures (see, for example, figure 14 of Coles) and aid light-attenuation studies in various flow configurations.

4. Conclusions

If the initial conditions of the equations describing the motion of an ellipsoidal particle in a viscous fluid are treated as random variables, then the probability density function of the Euler angles that describe the orientations of the flakes is adequate to explain the observed light field in flow-visualization experiments using such flakes. The flakes tend to align themselves with the stream surfaces, but their finite thickness causes rapid turnovers. Quantitative predictions are possible and the technique offers a new way of determining some flow properties as well as some suspension properties. This technique, however, seems to be unsuitable for visualizing low-amplitude waves in high shear flows, and due caution must be exercised in such applications.

The author extends his thanks to D. Coles, G. Emanuel, and P. Sepri for their constructive comments and illuminating discussions, and to K. Williams for her inexhaustable patience during the preparation of the manuscript.

REFERENCES

BATCHELOR, G. K. 1967 *An Introduction to Fluid Dynamics*. Cambridge University Press.

CANTWELL, B., COLES, D. & DIMOTAKIS, P. 1978 Structure and entrainment in the plane of symmetry of a turbulent spot. *J. Fluid Mech.* **87**, 641–672.

CARLSON, D. R., WIDNALL, S. E. & PEETERS, M. F. 1982 A flow-visualization study of transition in plane Poiseuille flow. *J. Fluid Mech.* **121**, 487–505.

CHAMBERS, F. W. & THOMAS, A. S. W. 1983 Turbulent spots, wave packets, and growth. *Phys. Fluids* **26**, 1160–1162.

COLES, D. 1965 Transition in circular Couette flow. *J. Fluid Mech.* **21**, 385–425.

GOLDSMITH, H. L. & MASON, S. G. 1962 Particle motions in sheared suspensions XIII. The spin and rotation of disks. *J. Fluid Mech.* **12**, 88–96.

GREENSPAN, H. P. 1968 *The Theory of Rotating Fluids*. Cambridge University Press.

JEFFERY, G. B. 1922 The motion of ellipsoidal particles immersed in a viscous fluid. *Proc. R. Soc. Lond.* A **102**, 161–179.

LEAL, L. G. & HINCH, E. J. 1971 The effect of weak Brownian rotations on particles in shear flow. *J. Fluid Mech.* **46**, 685–703.

LEAL, L. G. & HINCH, E. J. 1972 The rheology of a suspension of nearly spherical particles subject to Brownian rotations. *J. Fluid Mech.* **55**, 745–765.

PAPOULIS, A. 1984 *Probability, Random Variables, and Stochastic Processes*, 2nd ed. McGraw-Hill.

ROGERS, M. H. & LANCE, G. N. 1960 The rotationally symmetric flow of a viscous fluid in the presence of an infinite rotating disk. *J. Fluid Mech.* **7**, 617–631.

VAN DYKE, M. 1982 *An Album of Fluid Motion.* The Parabolic Press.

WEIDMAN, P. D. 1976 On the spin-up and spin-down of a rotating fluid. Part 2. Measurements and stability. *J. Fluid Mech.* **77**, 709–735.

WYGNANSKI, I., HARITONIDIS, J. H. & KAPLAN, R. E. 1979 On a Tollmien–Schlichting wave packet produced by a turbulent spot. *J. Fluid Mech.* **92**, 505–528.